JOURNAL OF AIRCRAFT
Vol. 41, No. 6, November–December 2004

Microactuators for Projectile Flight Control Systems: a Feasibility Study

Gjoko Apostolovski* and Yiannis Andreopoulos†
City College of the City University of New York, New York, New York 10031

New concepts for microactivated flight control of projectiles have been investigated for operation in both subsonic and supersonic flight regimes. A successful concept can provide an inexpensive flight control device with many control redundancies, and it can reduce size weight and energy consumption of the control system. Two promising concepts have been explored in detail. The first one consists of a microflap in the form of a delta wing of 3 mm base by 4 mm height, which can be deployed and activated at a location on the ogive of the projectile or at the beginning of its cylindrical afterbody. The second concept is based on microballoons, which can be inflated and change the local pressure distribution on the projectile. A computational-fluid-dynamics (CFD) computer code has been used to model these two flight control concepts. The first concept was tested at two angles of extension, 9 and 21 deg and at seven different flight Mach numbers: 0.3, 0.5, 0.7, 0.8, 1.0, 1.5, 2.0, and 3.0. Some additional cases with 150-deg extension angle were also investigated. The second concept based on microballoons was tested at four different Mach numbers: 0.6, 1.0, 1.8 and 2.2. Particular emphasis has been given in the CFD analysis in resolving the flow characteristics around the deployed control surfaces. Longitudinal vortices were found above the upper surface of the delta wing in all investigated Mach numbers, which reduce the pressure there and shock waves acting on the lower surface in the case of supersonic flights. The results show that the ratio of lift to drag of the control surface is about nine in the subsonic flow regime and about five in the supersonic flow regime. These values suggest that this control surface can provide adequate control force for possible maneuvering of the projectile. However, microactuators deployment was also found to increase the total drag of the projectile by 1 to 4%. In cases with deployment of two microactuators located next to each other, mutual interference affects favorably the aerodynamic control forces.

Nomenclature

C_d	=	drag coefficient
C_l	=	lift coefficient
C_m	=	moment coefficient
Cp_b	=	base-pressure coefficient
M	=	Mach number
R	=	projectile diameter
α	=	angle of attack (local)

I. Introduction

CONCEPTS of using microsensors and microactuators to control the flow over aerodynamic surfaces offer the potential of enhanced flight performance and maneuverability for the present and next generation of projectiles. Laboratory experiments with low-speed flows have demonstrated that microactuators can yield control of unsteady aerodynamics, reduced drag, enhanced lift, and increased control response.[1–3] All of these developments require better understanding of complex flowfields. Activation and deployment of surface-mounted microactuators introduce substantial perturbations in the flow that can cause separation of the boundary layer developing over the projectile surface, the appearance of shock waves in case of high-speed flows, and the generation of a large amount of vorticity shed off in the form of vortices, which can impact the downstream surface of the projectile and affect its performance. Thus, as a result of the mutual interaction between the boundary-layer flow developing around the projectile and the control surface, deterioration of the performance of the maneuvering projectile can be expected. The physics of the flow phenomena associated with the mutual interference between the control surface and the main body of the projectile is not well understood.

The objective of the present proposed work is to explore the possibility of using microflaps embedded on the exterior surface of projectiles like those shown in Figs. 1a–1c to provide active control in critical circumstances. Because of their sizes, microflaps can be actuated much more rapidly than conventional wing controls. This leads to higher bandwidth and response. Unlike conventional control surfaces, failure of some of these surfaces is not critical because many redundant surfaces are employed. In addition they can provide enhanced controlled forces for higher maneuverability. During flight without maneuvering, they remain undeployed in their cavity flush with the surface, and therefore their contribution to drag is minimal.

The outcome of the present work will provide information on the potential of using microactuators for flight control, the flow structure in the vicinity of the actuators, and their aerodynamic performance during operation under static conditions.

II. Computational Work

To demonstrate the potential of using microflaps for aerodynamic control, a feasibility study was carried out. In these computational studies, several numerical simulations were performed by solving the three-dimensional compressible Reynolds-averaged Navier–Stokes equations, which were coupled with the transport equation for energy. The preceding equations were solved numerically by using the solver FLUENT. The Spalart–Alamaras model[4] was used to simulate the effects of turbulence in the present study. The computations were carried on dual-processor platform with LINUX operating system. In these simulations the 105-mm Smart Cargo Round projectile, shown in Fig. 2a, with an ogival nose and a cylindrical afterbody was tested without its traditional flight control surfaces. Typical actuators assumed to be located in the nose, as shown in Fig. 2b, or at the beginning of the cylindrical afterbody so

Received 16 February 2003; revision received 20 November 2003; accepted for publication 24 November 2003. Copyright © 2004 by Yiannis Andreopoulos. Published by the American Institute of Aeronautics and Astronautics, Inc., with permission. Copies of this paper may be made for personal or internal use, on condition that the copier pay the $10.00 per-copy fee to the Copyright Clearance Center, Inc., 222 Rosewood Drive, Danvers, MA 01923; include the code 0021-8669/04 $10.00 in correspondence with the CCC.

*Research Assistant, Experimental Aerodynamics and Fluid Mechanics Laboratory, Department of Mechanical Engineering.

†Michael Pope Professor of Energy Research, Experimental Aerodynamics and Fluid Mechanics Laboratory, Department of Mechanical Engineering; andre@ccny.cuny.edu.

Table 1 Flow parameters and cases tested for the Smart Cargo Round 105 mm with delta-wing microflaps as actuators

	Mach number							
Cases tested	0.3	0.5	0.7	0.8	1.0	1.5	2.0	3.0
Two-dimensional axisymmetric	♦	♦	♦	♦	♦	♦	♦	♦
Three-dimensional no microflap (with $\alpha = 0$ deg)	♦	♦	—	♦	♦	♦	♦	♦
Three-dimensional microflap at $\alpha = 9$ deg	♦	♦	♦	♦	—	♦	♦	—
Three-dimensional microflap at $\alpha = 21$ deg	♦	♦	♦	♦	♦	♦	♦	—

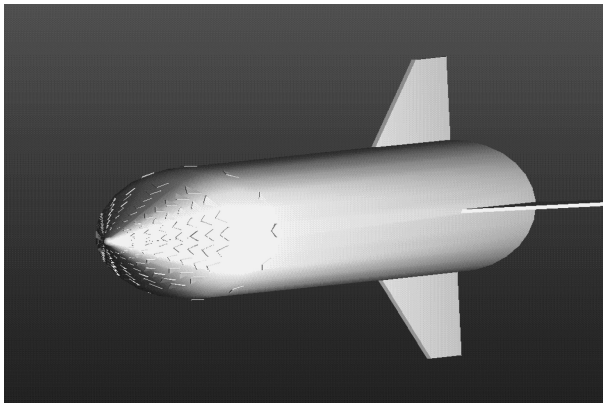

a)

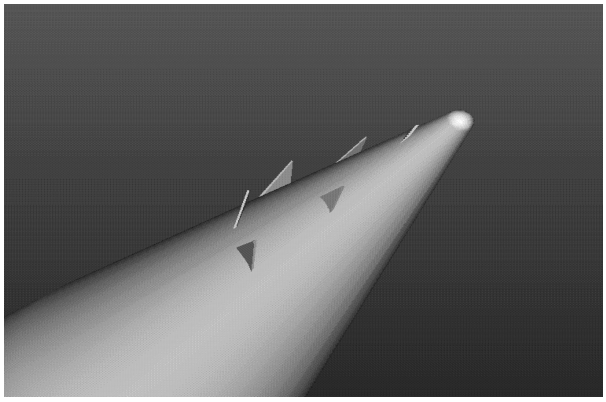

b)

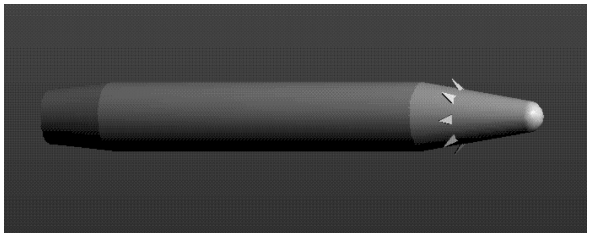

c)

Fig. 1 Microflap configurations.

that a sizeable moment could be obtained although the aerodynamic force generated by the microflap was small. Two types of actuators were used in the present investigation. First a delta-wing configuration was tested systematically. The second type of actuator tested here was an inflated balloon in the form of a bubble, which was used to deflect the flow. In addition, the delta-wing actuator was tested at two different locations. Some generic features of the flow interaction between the actuator and the developing boundary layer were studied in a simplified three-dimensional flowfield consisting of a delta-wing actuator embedded in a two-dimensional boundary layer developing over a flat plate.

A. Delta-Wing Microactuators

The shape of the microflaps used here is that of a delta wing with dimensions as shown in Fig. 2c. Steady-state calculations for turbulent flows were carried with the microflap extended at specific angles to the local surface while the projectile was kept always at zero angle of attack. Several cases were investigated at various flight Mach numbers M and extension angles α of the microflap. The case with $\alpha = 0$ deg provided a reference test case with only the drag force acting on the projectile. Base-pressure coefficient data obtained in these reference test cases were used to compare with experimental data. Table 1 shows the parameters used in the present investigation.

Typical results of velocity and pressure contours at Mach numbers 0.5 and 1.2 are shown in Figs. 3a–3d. These results have been obtained in the case of the axisymmetric configuration or in the case of three-dimensional calculations without the microflap. No major qualitative or quantitative differences were observed between these two cases. The major flow characteristics seem to have been captured in the present computations. The stagnation region at the nose of the projectile is clearly shown while the reverse flow in the near wake of the body (not shown here) is also correctly depicted. The results also show that the flow expands at the beginning and at the end of the cylindrical portion of the projectile and at the edge of the base. Results at Mach numbers 1.5 and 2.5 are shown in Figs. 3e–3h. Oblique shock waves are formed at the nose of the body as well as at the base. The shock waves bend downstream more at higher Mach numbers. Regions of flow expansion associated with the appearance of expansion waves are also observed here at the locations, where the cross-sectional area of the projectile changes to smaller values.

Experimental data obtained in the flow around the present projectile are not available yet. Thus, it was not possible to compare directly the values of quantities computed in the present work with similar data obtained experimentally. However it is possible to compare the present data with experimental data obtained not in the same projectile configuration but in similar cases. Although this type of comparison is not always meaningful, it is helpful in providing some indication of the quality of the data needed in the early stages of the design considerations. One data comparison is between the coefficient of base pressure data $[Cp_b = (\bar{p} - p_{\text{ref}})/1/2\rho U_0^2]$ obtained in the present work and those obtained experimentally in cases of square-based projectiles. Experimental data for various cases have been compiled by H. Hudgins of the Aeroballistics Branch at Picatinny Arsenal. Figure 3i shows a comparison of these data with the present results of the computational-fluid-dynamics (CFD) calculations. Such a comparison indicated differences from 5 to 20% between the present data and experiments. The largest difference was observed in the subsonic flow cases, and the smallest were observed in the supersonic flow cases. If one considers that the present Smart Cargo projectile has a tapered tail/base configuration, the fact that the present values are smaller in the transonic and supersonic regions is not surprising.

A very fine grid was used in the computations so that the flow details around the microflap could be captured and well resolved. Figure 4 shows the flow domain and meshing around the body. Unstructured grids with almost 4×10^6 tetrahedral elements were used in the present computations. The results obtained were tested for grid independence, which is a standard demonstration of numerical accuracy involved in the computations. Grid independence is difficult to apply for calculations of wall-bounded flows because the near-wall grid has to match the requirements of the near-wall model. In the present case most of the drag on the actuators is pressure drag

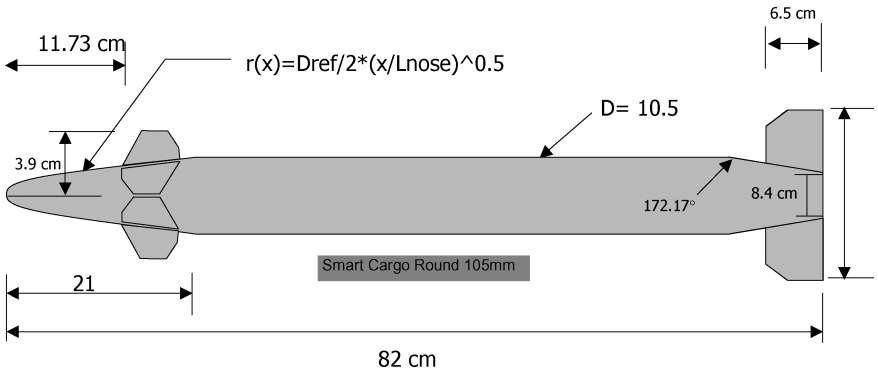

Fig. 2a Initial configuration of Smart Cargo Round 105 mm.

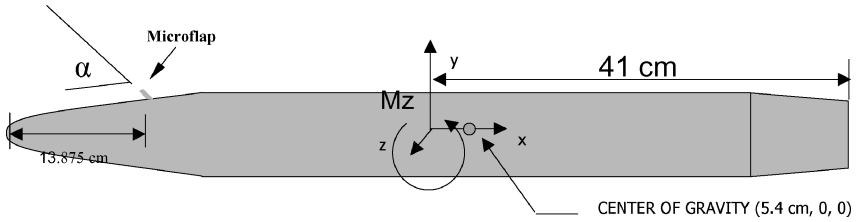

Fig. 2b Tested configuration of Smart Cargo Round 105 mm with one microflap.

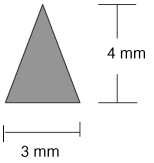

Fig. 2c Microflap geometry.

rather than drag caused by viscous forces, although grid points near the wall resolved adequately the wall viscous layer. The solutions obtained in the present tests with three different grid sizes yielded values of forces within 0.7% from each other.

Results for the $M = 0.5$ and $\alpha = 9$ deg case are shown in Figs. 5a–5d. Figure 5a shows the contours of the longitudinal velocity distribution on the plane of symmetry, whereas Fig. 5b shows the velocity distribution around the microflap. There is some stagnation region in front of the delta wing, and the flow seems to expand in the back of it. The pressure distribution around the microflap is shown in Fig. 5c. High pressure in front of it and low pressure behind it are the major characteristics of this distribution, which can be used to estimate the structural strength of the device. Figure 5d shows the velocity vectors on a plane normal to the longitudinal direction in the wake of the microflap. A large vortical motion is evident in this figure, which suggests that the flowfield around the extended microflap is complicated.

At higher Mach numbers, the pressure load around the microflap increases substantially. This is evident in Fig. 6a, where the pressure distribution around the microflap is shown for the case of $M = 0.8$ and $\alpha = 9$ deg. The pressure in the stagnation region is about 130 kPa, whereas the pressure in the case of $M = 0.5$ shown in Fig. 5c is 10 times less. It appears that a shock wave is formed in front of the extended device, which increases substantially the pressure behind it.

The flowfield in the back of the microflap is accelerated rapidly, and velocity values up to 600 m/s have been computed. A shock wave appears to be formed at the back root of the microflap.

At higher extension angles α of the microflap, the flowfield is qualitatively and quantitatively different than in the case with $\alpha = 9$ deg. Figures 7a and 7b show the pressure and velocity distribution respectively around the microflap, which is now extended to $\alpha = 21$ deg. The flow appears to gradually decelerate in the stagnation region formed in front of the device, a behavior, which indicates the lack of shock-wave appearance. There is a strong secondary flow in the cross-sectional plane behind the microflap, which suggests the existence of vortices that are characteristically formed over delta wings. The velocity vectors shown in Fig. 7c also indicate some opposite rotational motion associated with the vorticity of the incoming boundary layer, which appears to wrap around the base of the protruded microflap device.

At higher Mach numbers the same geometrical configuration behaves differently. Figures 8a–8c show the pressure and velocity distribution in the vicinity of the microflap at $M = 2$ and $\alpha = 21$ deg. These figures clearly indicate the existence of a three-dimensional shocked region formed in the region upstream of the microflap in the region where the flow stagnates. The shock starts at the apex of the delta wing, and it is extended down to the wall region of the main body of the projectile. There is also a weak shock formed at the back of the microflap.

The coefficients of the lift and drag forces acting on the microflap are plotted in Figs. 9a and 9b. The values of C_l and C_d are referenced to the cross-sectional area of the projectile. It is clear that when the microflap is extended further into the flow the nondimensional forces in the normal and longitudinal directions are larger. However, the ratio C_l/C_d is larger at smaller α in all Mach numbers investigated, as shown in Fig. 9c.

Figure 9d shows the overall drag coefficient for the projectile and the drag penalty when the microflaps are extended. The drag coefficient data for $\alpha = 0$ deg are also compared with the experimental values of the M483A1 round, which has comparable dimension with the present Smart Cargo configuration. The present data appear to be about 10 to 20% higher than the experimental values of the M483A1 round. This could be attributed to the fact that the present calculations were carried out by assuming that the boundary layer and the wake are turbulent because transition from laminar to turbulent flow was not considered. Although this difference is not entirely meaningful because the comparison is between two rather different projectiles, it can be considered as indicative of the accuracy of the CFD calculations. The data on this figure also show how the microflap interferes with the flow over the projectile and how its performance is affected by the extended microflap. This is also shown in Fig. 9e, where values of the ratio of the overall lift to drag forces acting on the projectile are plotted against Mach number. According to the coordinate system and definitions adopted in the present investigation, negative lift is in the negative y direction, and a positive moment coefficient C_m indicates a nose-down motion. The data in Fig. 9e indicate that normal forces of a few percent

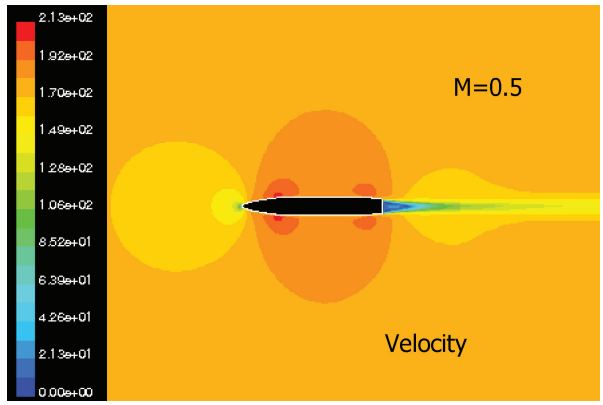

a)

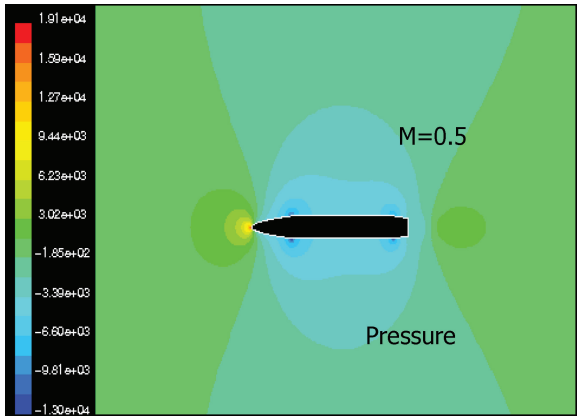

b)

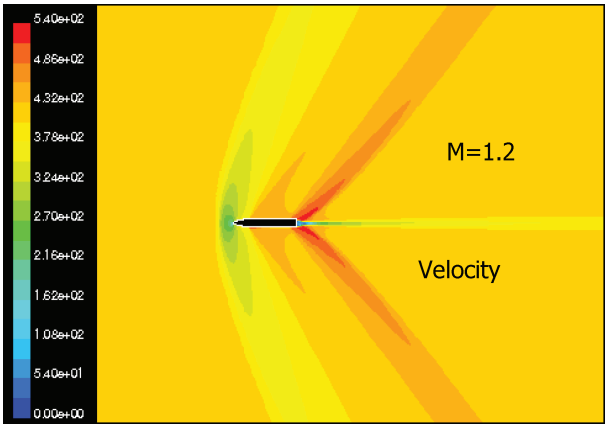

c)

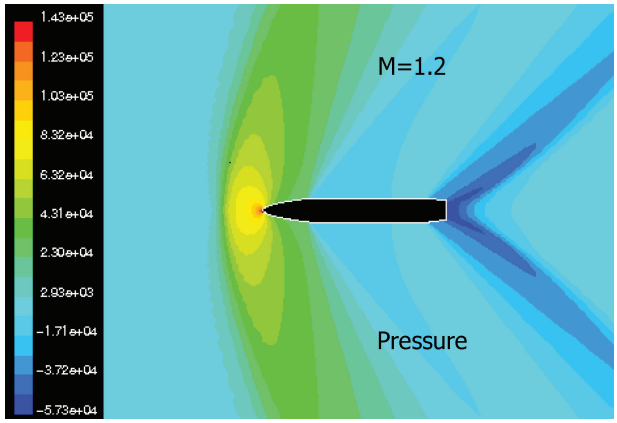

d)

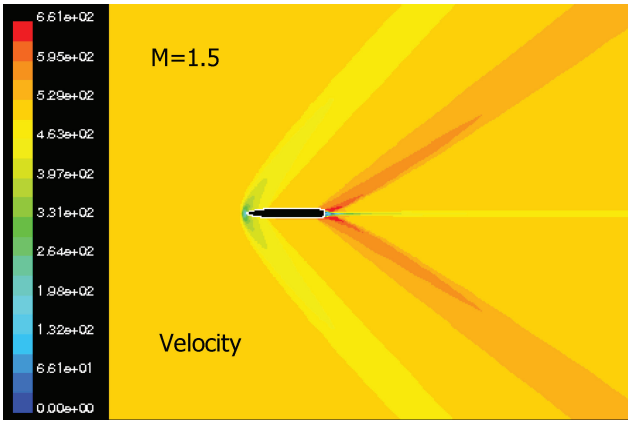

e)

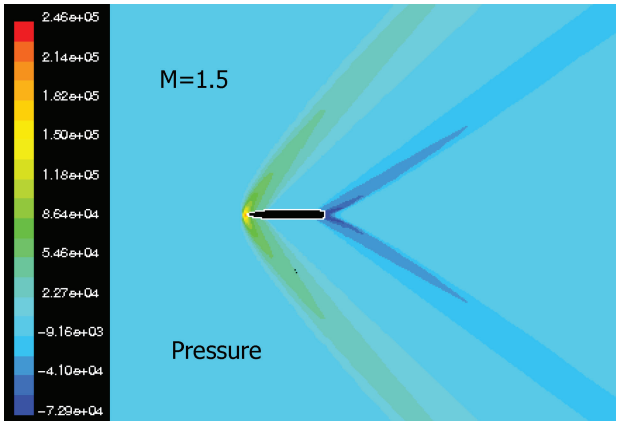

f)

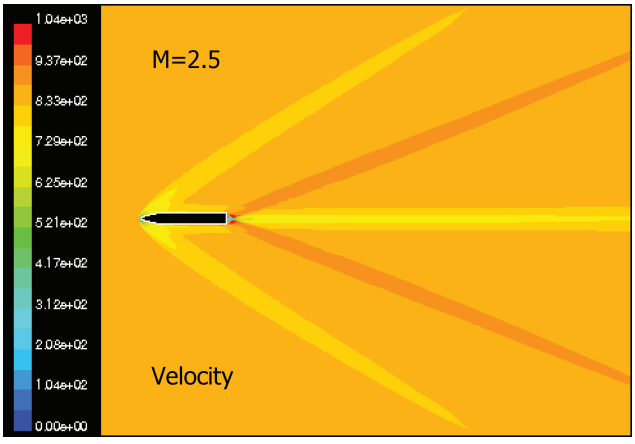

g)

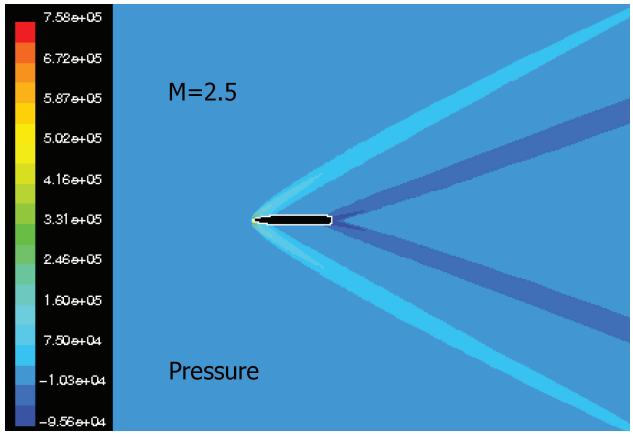

h)

Fig. 3 Velocity and pressure distribution along the symmetry plane of projectile at various Mach numbers: a)–h).

of the drag force can be generated by one microflap. The sign of the control force appears to change at supersonic Mach umbers. Of importance is, however, the overall moment coefficient C_m, which expresses the control moment about the center of gravity acting on the whole projectile. Values of C_m obtained in the present computations are plotted in Fig. 9f. Control with $\alpha = 9$ deg appears to result in higher values of C_m than in the case of control with $\alpha = 21$ deg in all subsonic Mach numbers. At supersonic Mach numbers values of C_m are about the same in both cases with the exception of C_m at $M = 1.5$, where it changes sign.

B. Inflated Balloon/Bubble Microactuators

A new type of microactuator called bubble actuator (Ref. 5) has been recently developed and tested in static wind-tunnel experiments.[2] A balloon made out of silicone rubber membrane is inflated by a pneumatic device and in its final formation can act as a flow deflector. This type of microactuator, which appears to be more robust than microelectromechanical-systems-based microflaps, has been also tested in the present investigation. The location and dimensions of this actuator were comparable to those used in the case of delta wings based microflaps (see Fig. 10a). Steady-state compressible Navier–Stokes solutions were also obtained by using the Fluent solver. The three-dimensional inflated balloon/bubble actuators were tested at Mach numbers of 0.6, 1.0, 1.8, and 2.2.

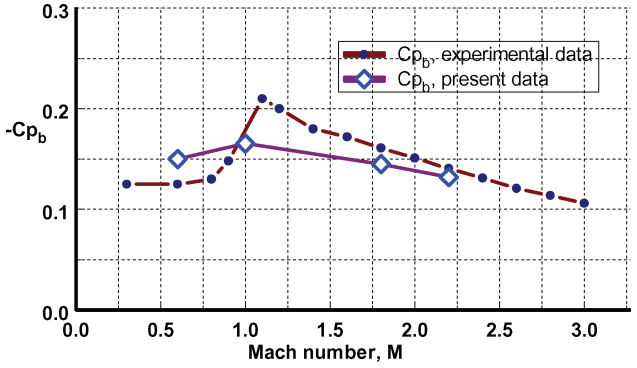

Fig. 3i Base-pressure coefficient. Comparison of present data with compiled experimental data for square-based bodies.

Figures 10b and 10c show some typical pressure distribution around the bubble at Mach umbers 0.6 and 1.0, respectively. Both cases show a high-pressure region upstream of the bubble where the flow is deflected and an expanding flow region in the back of the bubble where the flow accelerates substantially as it turns around the bubble. The presence of the wall, however, restricts further expansion, and the flow is decelerated in the immediate vicinity of the wake of the bubble. Integration of the pressure and viscous forces acting on the projectile and on the bubble results in the data of the ratio of the overall force in the normal direction to that in the longitudinal direction shown in Fig. 10d. Very small positive lift forces appear to be generated in subsonic and transonic flow Mach number and rather strong forces, of the order of 5% of the overall drag force, have been calculated in the supersonic cases. The data shown in Fig. 10d are also compared with the data obtained in the case of the delta-wing actuators. Data of the moment coefficient C_m have been plotted in Fig. 10e. The data for the case of the bubble actuator change sign at $M = 1$ indicating positive values of C_m (nose-down motion) for supersonic Mach numbers and negative values for subsonic Mach numbers. The data in Fig. 10e also show that this behavior of the bubble actuator is almost the opposite of the behavior of the delta-wing actuators extended at $\alpha = 21$ deg. Thus, it appears that both types of actuators can provide small forces and moments for flight control of projectiles.

C. Microactuators and the Boundary Layer

A typical actuator with a characteristic length h, which is considered for flight control of projectiles, appears to be of the same order of magnitude as the thickness δ of the boundary layer that is developing over the length of the projectile. For typical cases like the present ones, the thickness of the boundary layer developing over a length of $L = 1$ m is between 0 and 2 mm for the case of laminar

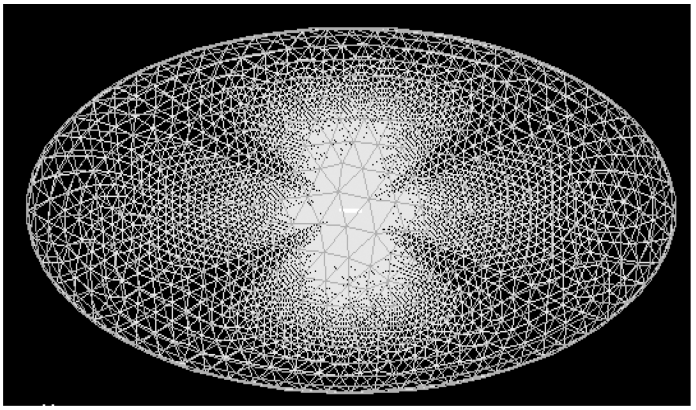

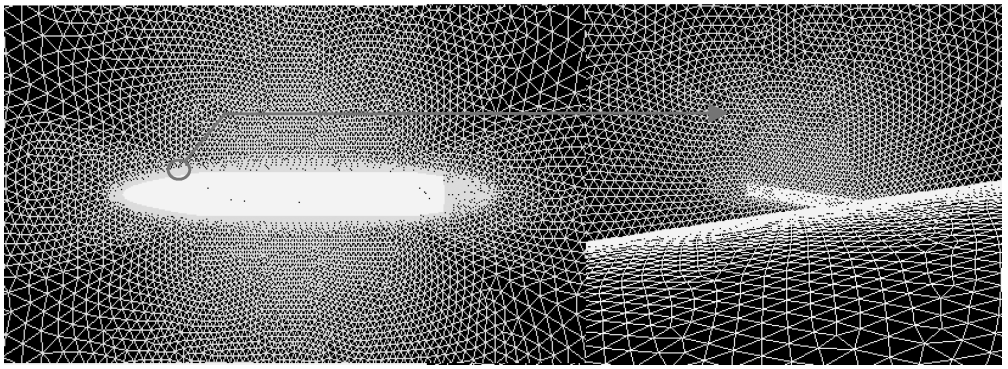

Fig. 4 Flow domain and meshing in three-dimensional calculations.

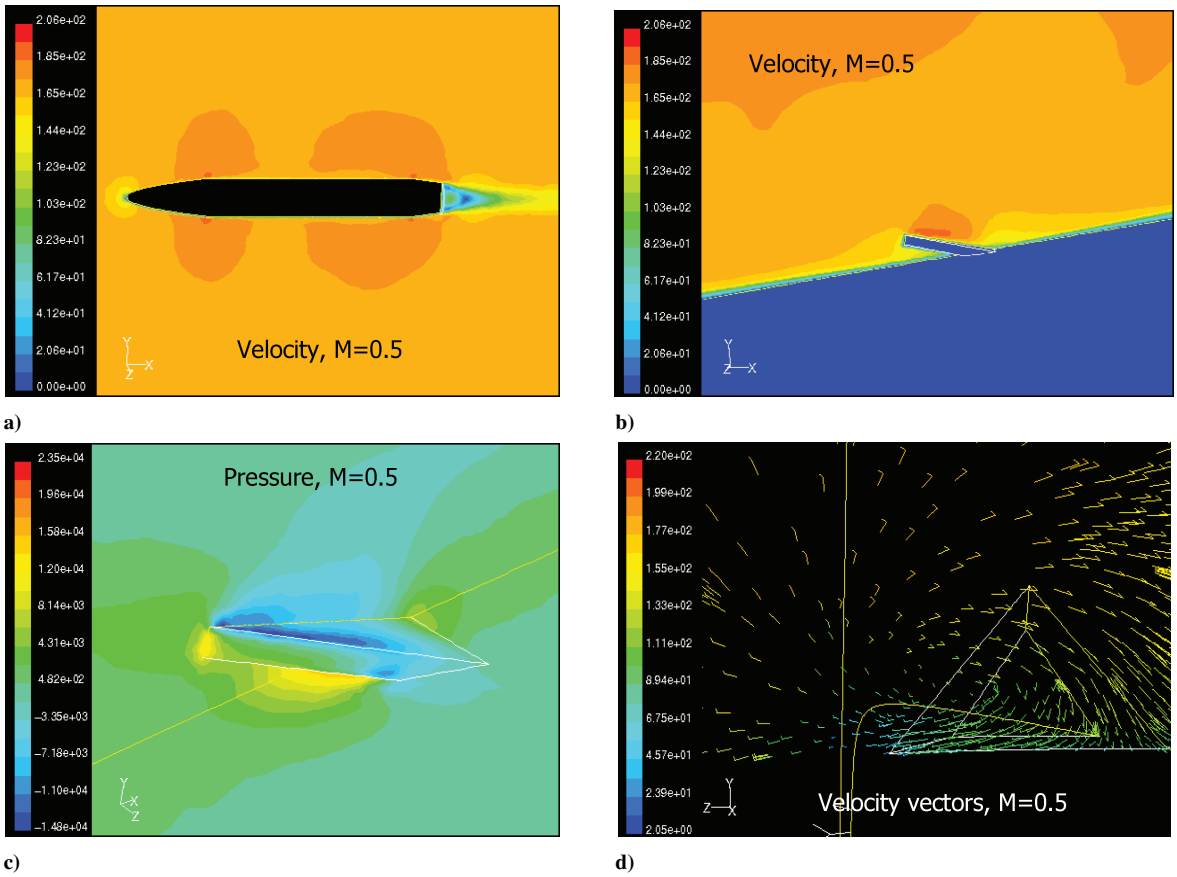

Fig. 5 Results of three-dimensional calculations for $M = 0.5$ and $\alpha = 9$ deg.

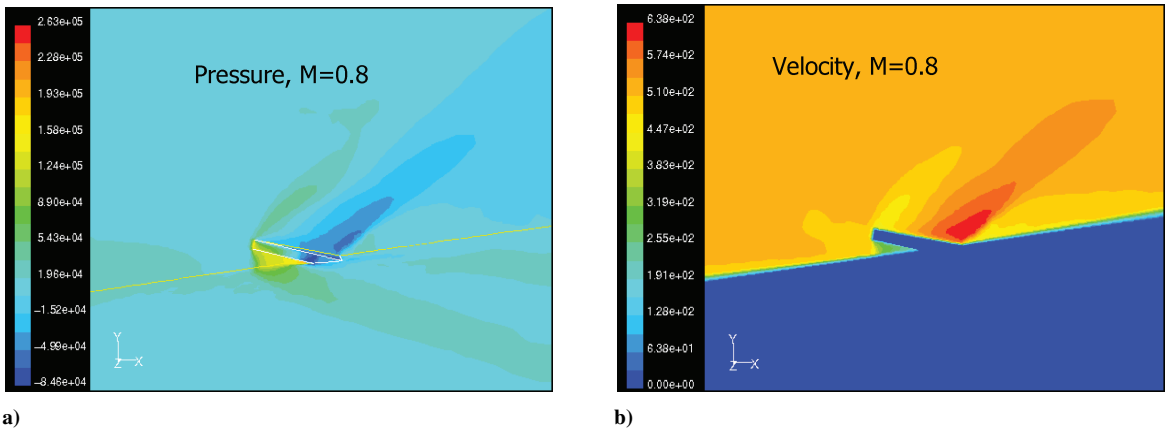

Fig. 6 Results of three-dimensional calculations for $M = 0.8$ and $\alpha = 9$ deg.

layers and between 0 and 8 mm for turbulent boundary layers. In cases where $h \ll \delta$ and with h of the order of the near-wall viscous length scale, active control of an actuator can interfere with the near-wall turbulent flow and reduce the skin friction. However, in cases where h is of the order of δ, the performance of the actuator can be affected by the boundary layer. To better understand the behavior of delta-wing microflaps and their interaction with the boundary layer some numerical experiments were carried out with delta-wing microflaps embedded in zero-pressure-gradient two-dimensional turbulent boundary layers. Although these runs were intended to reveal some basic characteristics of the flowfield, they could also be used as representative cases of the flow around microflaps located at the beginning of the cylindrical section of the projectile afterbody, where the ratio of the later curvature of the body ($R = \frac{105}{2} = 52$ mm) is significantly higher than the boundary-layer thickness, which is estimated to be of the order of 1 to 2 mm at this location.

The flow cases, which were investigated, are shown in Table 2. The flow domain and grid meshing are shown in Fig. 11a. Two different delta-wing geometries were tried. Delta wing 1 had a height of 4 mm and delta wing 2 had a height of 6 mm (see Fig. 11b). The flowfield with an actuator at a new angle $\alpha = 150$ deg was investigated in detail as well as the case of two delta wings located next to each other at $\alpha = 18$ deg.

Figure 11c shows the velocity magnitude contours in the vicinity of the microflap for the case with $\alpha = 150$ deg and $M = 0.5$. The lower half of the figure represents the flow without the microflap. The developing boundary layer over the flat plate is visible in this figure. The flow upstream of the delta wing appears to be deflected upwards, and the same time is decelerated in the longitudinal direction. A region of high static pressure is formed in front of the actuator with varying pressure distribution above and a lower pressure in the back of it (see Fig. 11d). The Mach-number distribution at locations

Table 2 Flow parameters and cases tested in flat-plate boundary layers with delta-wing microflaps as actuators

	Mach number				
Cases tested	0.5	0.7	0.8	1.0	1.2
Three-dimensional delta wing 1 (with $\alpha = 150$ deg)	♦	♦	♦	♦	♦
Three-dimensional delta wing 2 (with $\alpha = 30$ deg)	♦	♦	♦	♦	♦
Three-dimensional two delta wings 1 (with $\alpha = 18$ deg)	♦	♦	♦	♦	♦
Three-dimensional delta wing 1 (with $\alpha = 30$ deg)	♦	—	—	—	—
Three-dimensional delta wing 1 (with $\alpha = 30$ deg) in uniform flow (no wall)	♦	—	—	—	—
Three-dimensional two delta wings 1 (with $\alpha = 30$ deg)	♦	—	♦	—	♦

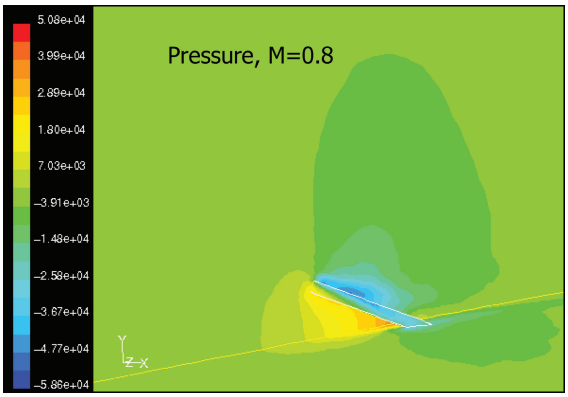

a)

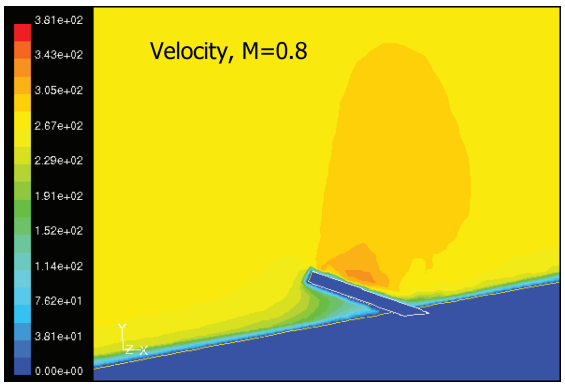

b)

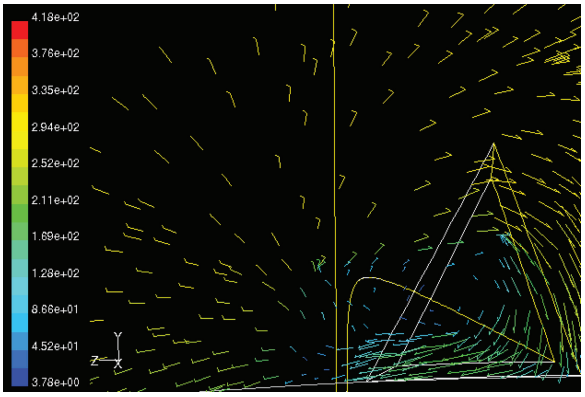

ptc)

Fig. 7 Results of three-dimensional calculations for $M = 0.8$ and $\alpha = 21$ deg.

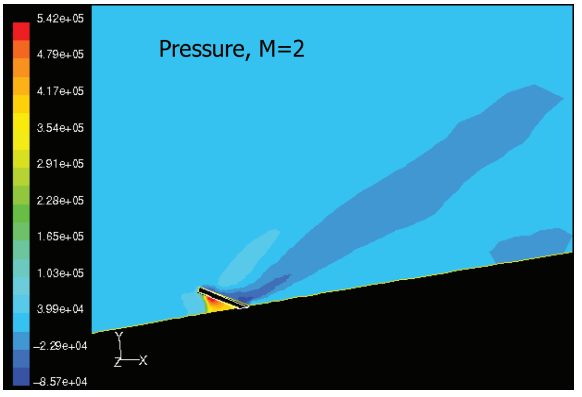

a)

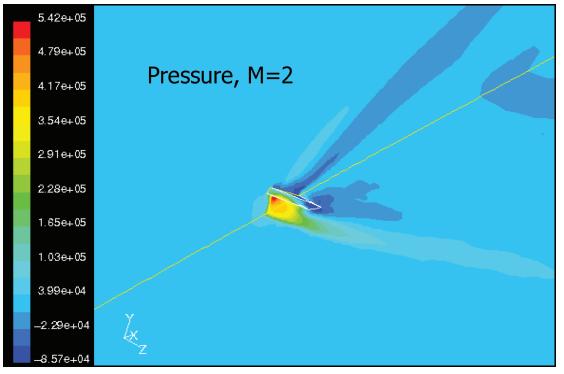

b)

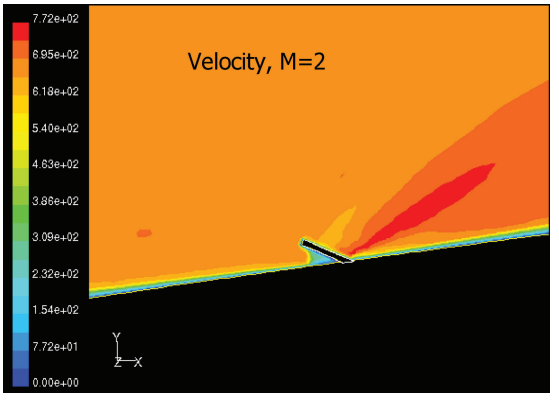

c)

Fig. 8 Results of three-dimensional calculations for $M = 2$ and $\alpha = 21$ deg.

a few mesh points above the solid surface of the wall and the actuator is shown in Fig. 11e. A low-speed streak in the near wake is evident in the picture. The flow is also accelerated at downstream distances in the wake, a feature that is still apparent at a distance from the actuator $5 \times$ height h. The secondary flow picture in the wake of the actuator, shown in Fig. 11f, depicts some significant details of the flow motion on this plane normal to the longitudinal direction. There is an inrush of fluid from above towards the wall, which seems to have been displaced by the presence of the delta wing. The incoming flow goes outwards and around the actuator and then it turns inwards towards the central plane in the wake of it. Two recirculating zones can be seen in this figure. The flow structure observed here has several similarities with the experimental results of Jeon and Blackwelder[6] who used large piezoceramic actuators to perturb the boundary layer in an attempt to reduce near-wall friction.

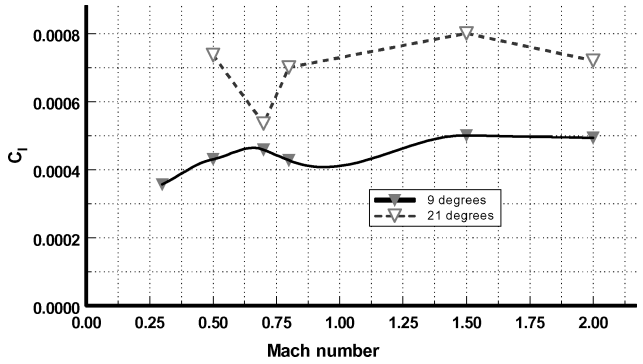

Fig. 9a Lift coefficient of microflap device.

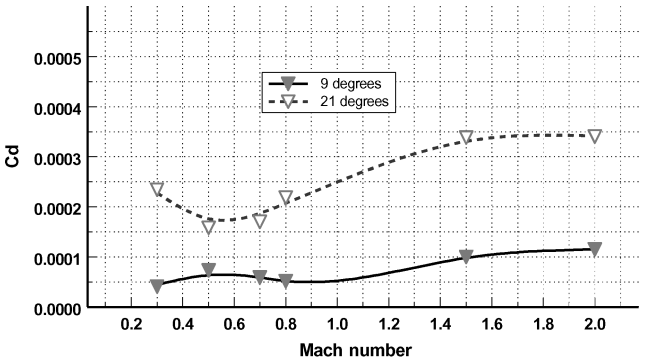

Fig. 9b Drag coefficient of microflap device.

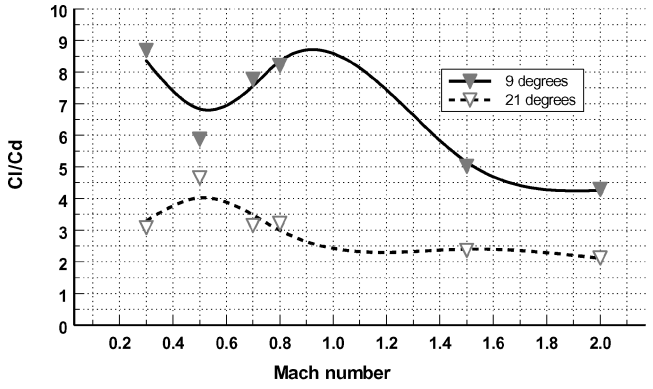

Fig. 9c Lift-to-drag ratio of microflap devices.

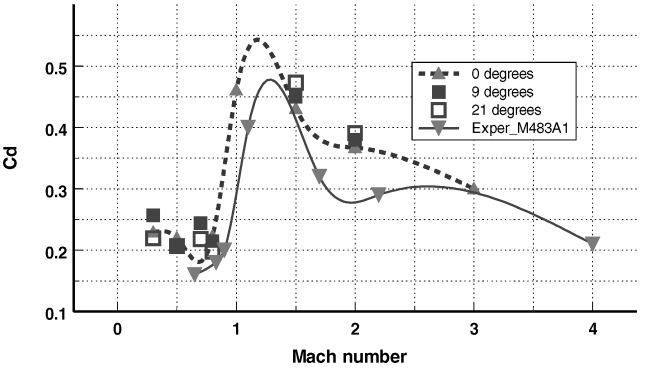

Fig. 9d Drag coefficient and comparison with experimental data.

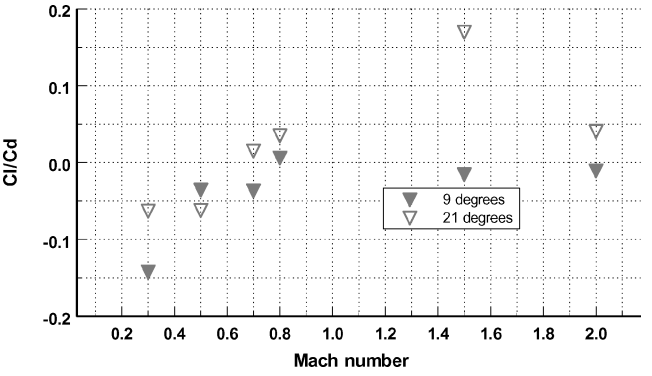

Fig. 9e Total lift-to-drag ratio.

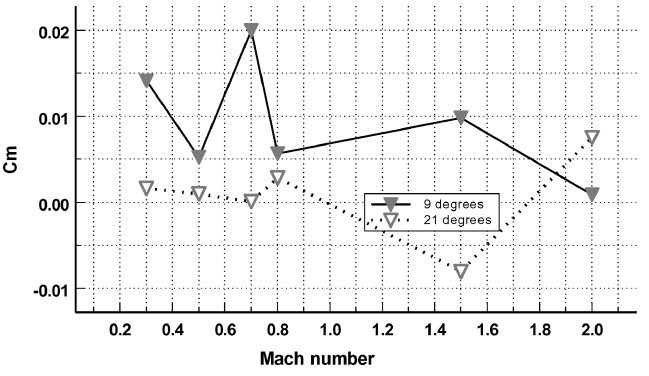

Fig. 9f Total-moment coefficient.

The flow pattern of the two vortices formed downstream of the actuator extended to $\alpha = 150$ deg from the upstream wall is different from the flow pattern formed by an actuator extended at $\alpha = 30$ deg. Figure 12a shows the Mach-number distribution for this case. A stronger wake is formed with two distinct low-speed streaks evident on both sides of the wake, which might indicate the existence of a horseshoe vortex with vorticity of the same sign like that of the incoming boundary layer. The secondary flow patterns of Fig. 12b show clearly the existence of two rotational motions in the wake and above the actuator that are know to form above delta wings.[7] At the plane of symmetry, the flow is directed towards the wall and then is diverted away from the plane of symmetry in the lateral direction. There some evidence of rotational flow with opposite vorticity to that of the other detached rotational flow over the delta wing, which might support the argument of existence of the horseshoe vortex.

To demonstrate the effects of the wall presence on the delta-wing flow, a reference case was computed with the wing inside a uniform freestream at Mach number $M = 0.5$. Because the same grid was used in these calculations without the wall and in the case of the delta wing in the presence of boundary layer developing over the wall, the results between these two cases can be compared directly. It was found that the presence of the wall increased the lift coefficient C_l by 36.5%, the drag coefficient C_d by 16.5%, and the ratio C_l/C_d by 17% over the case of a delta wing in a uniform flow. It appears that the presence of the wall causes the flow below the wing to stagnate and therefore increase the pressure on the wing that results higher drag and lift than in the case of a delta wing in a uniform flow where no flow stagnation takes place.

Of interest is the flowfield formed by the extension of two actuators at the same time into the flowfield. Figure 12c shows contours of the Mach-number distribution in the case of $M = 0.5$ and $\alpha = 18$ deg. These data clearly indicate the degree of interference that exists between the two actuators. For two delta wings placed far apart one should expect to observe four low-speed fluid streaks. Instead, two strong and one weak low-speed fluid streaks can be observed in the present case. The two strong streaks emanate from the two outer edges of the root of each actuator, a feature suggesting that the two units behave like a single one of twice the width of one actuator. The third low-speed fluid streak is formed in the area between the two wings. By looking at at the secondary flow shown in Fig. 12d, one can see that this weak streak is associated with the common flow between two strong rotational motions, which are present in the region between the two actuators. This common flow region brings fluid upwards away from the wall. The other classical vortices associated with outer leading edges of the two delta wings are also there, but their rotation appears to be weaker.

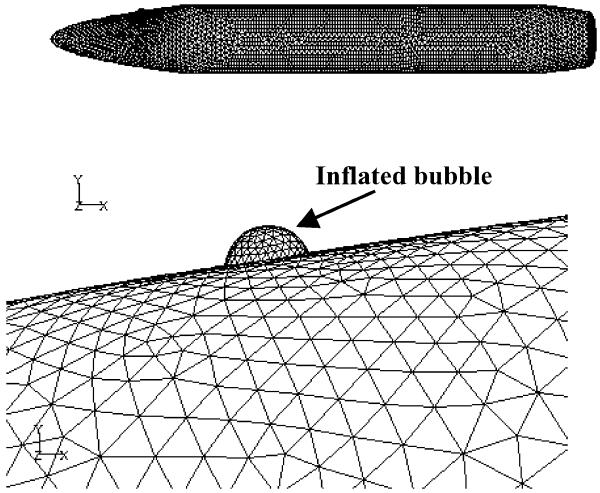

Fig. 10a Inflated bubble actuator, location and meshing.

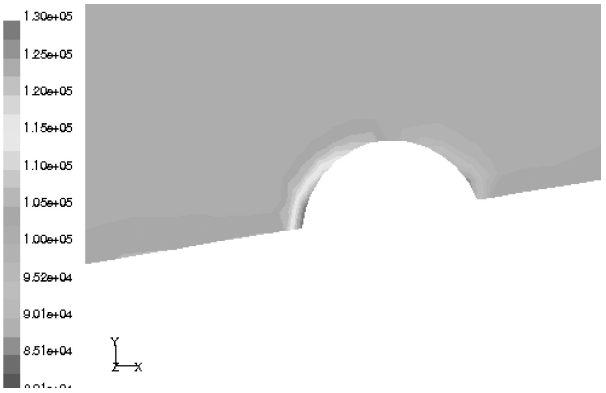

Fig. 10b Pressure distribution around bubble actuator for $M = 0.6$.

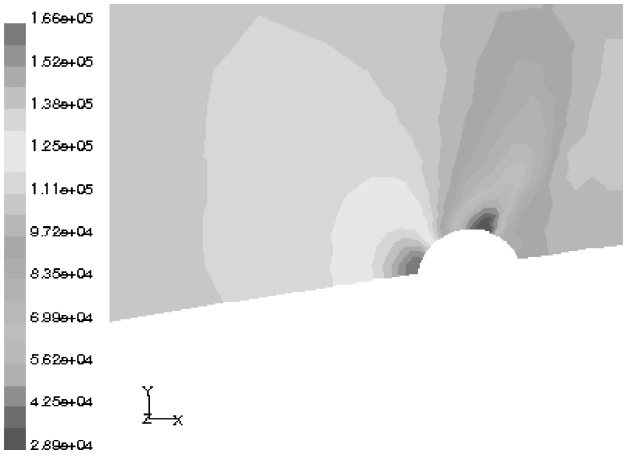

Fig. 10c Pressure distribution around bubble actuator for $M = 1.0$.

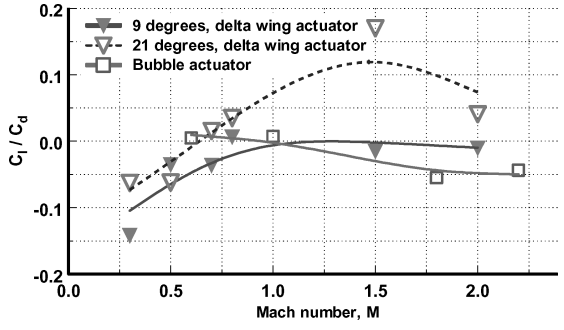

Fig. 10d Comparison of performance parameters of various actuators.

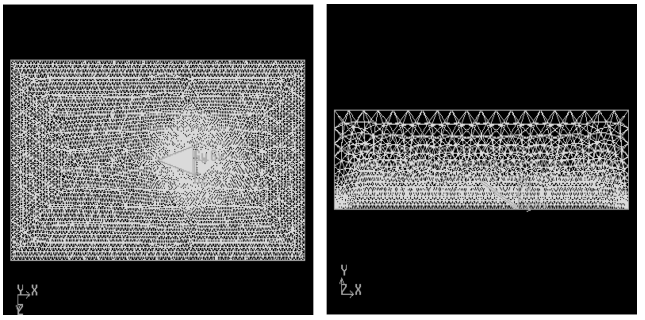

Fig. 11a Flow domain and meshing.

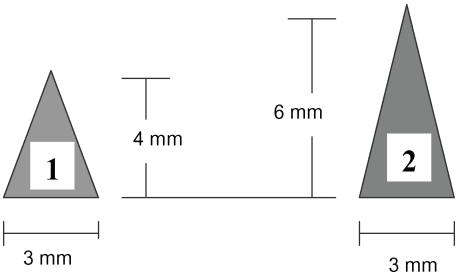

Fig. 11b Delta-wing actuators tested.

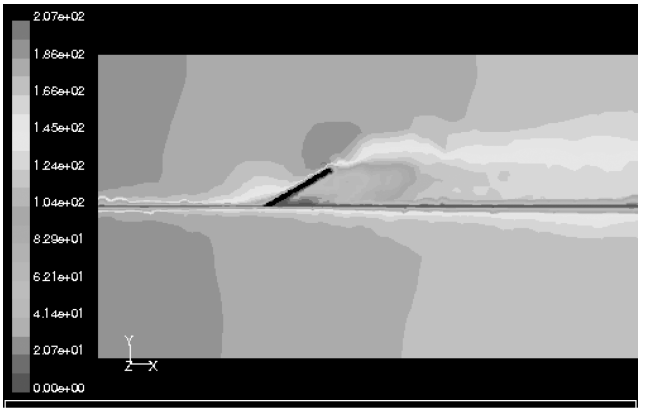

Fig. 11c Velocity contours for delta wing 1 at $M = 0.5$ and $\alpha = 150$ deg. Flow from left to right.

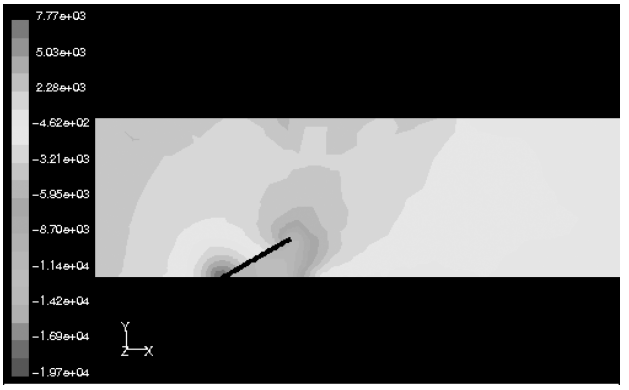

Fig. 11d Static-pressure contours for delta wing 1 at $M = 0.5$ and $\alpha = 150$ deg.

Near the wall to the left and right of the delta wings, a low-speed region exists, which is associated with the slow-speed fluid streaks that wraps around the two actuators. Most probably this is caused by the trace of the horseshoe vortex system that is formed by the separation of the incoming boundary layer.[8]

Figure 12e shows the ratio of the lift-to-drag forces acting on the actuators. For the case of the actuator with $\alpha = 150$ deg, this ratio is negative indicating that the upward extension of the microflap

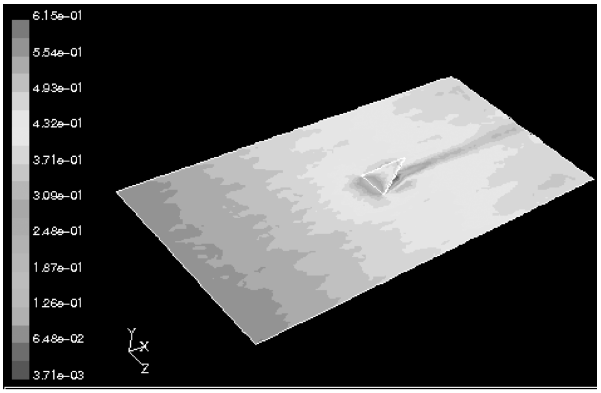

Fig. 11e Mach-number contours at locations off the solid surfaces for delta wing 1 at $M = 0.5$ and $\alpha = 150$ deg.

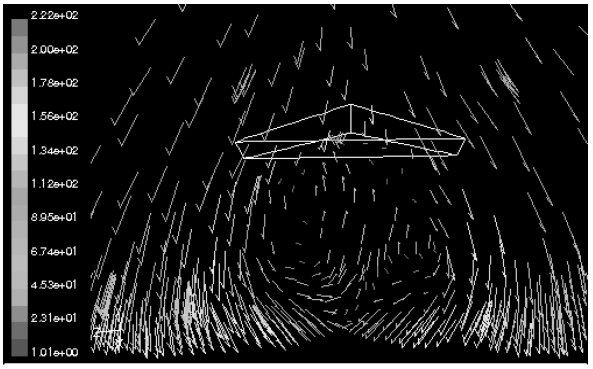

Fig. 11f Secondary flow on a plane in the wake of the actuator normal to the wall. Case with delta wing 1 at $M = 0.5$ and $\alpha = 150$ deg.

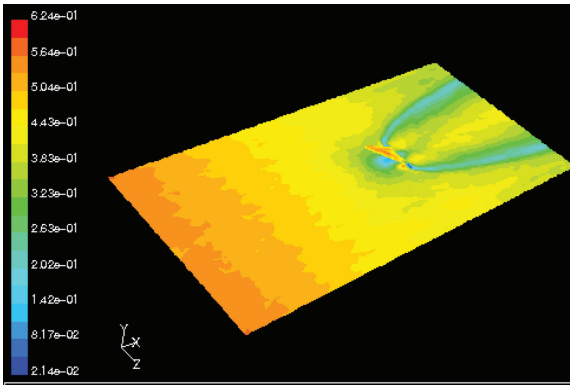

Fig. 12a Mach-number contours at locations off the solid surfaces for delta wing 2 at $M = 0.5$ and $\alpha = 30$ deg.

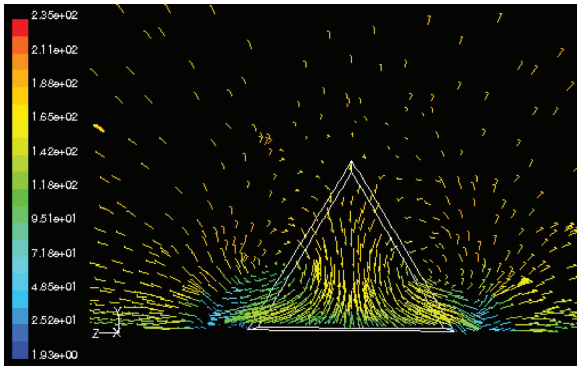

Fig. 12b Secondary flow on a plane in the wake of the actuator normal to the wall. Case with delta wing 2 at $M = 0.5$ and $\alpha = 30$ deg.

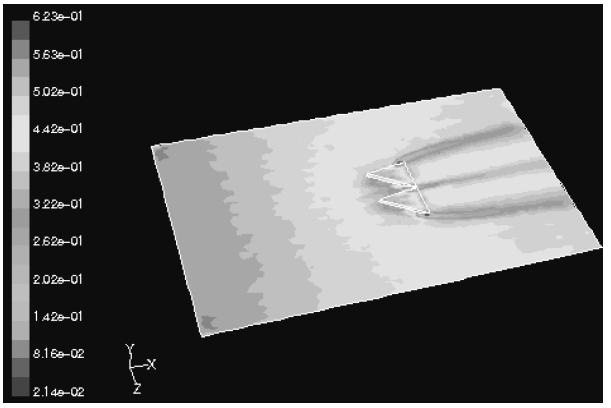

Fig. 12c Mach-number contours at locations off the solid surfaces for delta wing 2 at $M = 0.5$ and $\alpha = 18$ deg.

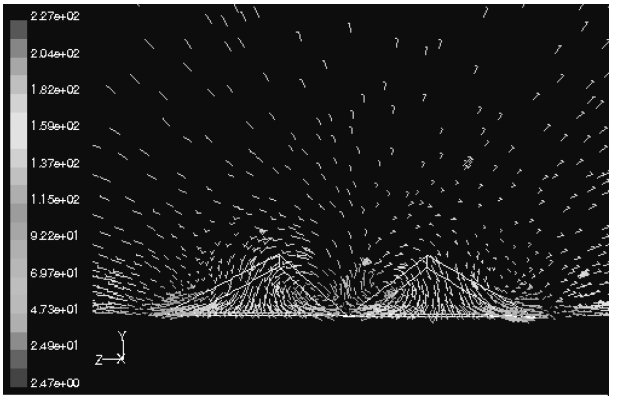

Fig. 12d Secondary flow on a plane in the wake of the actuators normal to the wall. Case with delta wing 2 at $M = 0.5$ and $\alpha = 18$ deg.

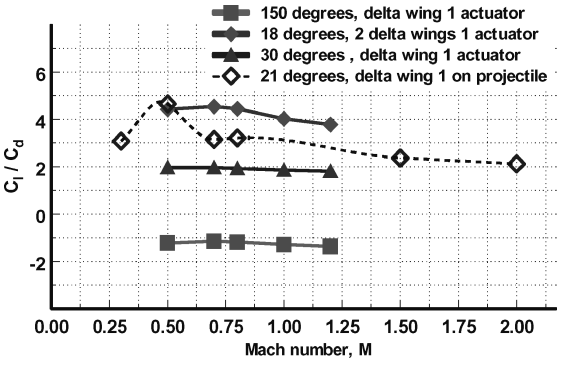

Fig. 12e Ratio of lift-to-drag forces acting on actuators.

will result in a downward force (negative lift). The actuator with extension angle $\alpha = 21$ deg has positive values of C_l/C_d ratio as expected. If this case is compared to the single actuator case at $\alpha = 18$ deg, an estimate of the degree of interference can be obtained. For instance, in the case of a single actuator located on the projectile at $M = 0.8$ a value $C_l/C_d = 2.5$ can be observed. For two actuators the actual computed value is about 4.5, which indicates 80% increase of performance as a result of mutual interference or as a result of the flow divergence in the conical nose of the projectile.

III. Conclusions

Our literature review and work have indicated that the use of microactuators for flight control systems might be feasible and realizable. New concepts for microactivated flight control of projectiles have been investigated for operation in both subsonic and supersonic flight regimes by using computational-fluid-dynamics (CFD) analysis. Two promising concepts have been explored in detail. The first one consists of a microflap in the form of a delta wing of 3-mm base

by 4-mm height, which can be deployed and activated at a location on the ogive of the projectile or at the beginning of its cylindrical afterbody. The second concept is based on microballoons, which can be inflated and can change the local pressure distribution on the projectile.

The first concept was tested at two angles of extension, 9 and 21 deg and at seven different flight Mach numbers: 0.3, 0.5, 0.7, 0.8, 1.0, 1.5, 2.0, and 3.0. Some additional cases with 30- and 150-deg extension angle were also investigated. The second concept based on microballoons was tested at four different Mach number: 0.6, 1.0, 1.8, and 2.2. Particular emphasis has been given in the CFD analysis in resolving the flow characteristics around the deployed control surfaces. Longitudinal vortices were found above the upper surface of the delta wing in all investigated Mach numbers, which reduce the pressure there and shock waves acting on the lower surface in the case of supersonic flights. The results show that the ratio of lift to drag of the control surface is about nine in the subsonic flow regime and about five in the supersonic flow regime. These values suggest that this control surface can provide adequate control force for possible maneuvering of the projectile. However, microactuators deployment was also found to increase the total drag of the projectile by 1–4%. In cases with deployment of two microactuators located next to each other, mutual interference affects favorably the aerodynamic control forces.

Acknowledgments

The present work was supported by Army Research and Development Engineering Center (ARDEC)-Picatinny Arsenal through Contract # DAAE30-01-M1093 monitored by Greg Bisher. Henry Hudgins of the Aeroballistics Branch at Picatinny Arsenal provided a compiled dataset of experimental data on base pressure.

References

[1]Folk, C., and Ho, C.-M., "Micro-Actuators for Control of Delta Wing with Sharp Leading Edge," AIAA Paper 2001-0121, Jan. 2001.

[2]Huang, A., Folk, C., Silva, C., Christensen, B., Chen, Y., and Ho, C.-M., "Micro-Actuators for Control of Delta Wing with Sharp Leading Edge," AIAA Paper 2001-0124, Jan. 2001.

[3]Ho, C.-M., and Tai, Y.-C., "Micro-Electro-Mechanical-Systems (MEMS) and Fluid Flows," *Annual Review Fluid Mechanics*, Vol. 30, 1998, pp. 579–612.

[4]Spalart, P., and Alamaras, S., "A One-Equation Turbulence Model for Aerodynamic Flows," AIAA Paper 92-0439, Aug. 1992.

[5]Grosjean, C., Lee, G. B., Hong, W., Tai, Y. C., and Ho, C. M., "Micro Balloon Actuators for Aerodynamic Control," *Proceedings of the IEEE-MEMS Workshop*, Germany, 1998.

[6]Jeon, W.-P., and Blackwelder, R. F., "Perturbations in the Wall Region Using Flush Mounted Piezoceramic Actuators," *Experiments in Fluids*, Vol. 28, 2000, pp. 485–496.

[7]Honkan, A., and Andreopoulos, J., "Instantaneous Three Dimensional Vorticity Measurements in Vortical Flow over a Delta Wing," *AIAA Journal*, Vol. 35, No. 10, 1997, pp. 1612–1620.

[8]Agui, J. H., and Andreopoulos, J., "Experimental Investigation of a Three Dimensional Boundary Layer Flow in the Vicinity of an Upright Wall Mounted Cylinder," *Journal of Fluids Engineering*, Vol. 114, No. 4, 1992, pp. 566–576.